Vehicular MIMO SAR Imaging in Multipath Environments

by

Li Li

Department of Electrical and Computer Engineering
Duke University

Date:_____

Approved:

_____
Jeffrey L. Krolik, Advisor

_____
Loren W. Nolte

_____
Matthew S. Reynolds

Thesis submitted in partial fulfillment of
the requirements for the degree of Master of Science
in the Department of Electrical and Computer Engineering
in the Graduate School
of Duke University

2011

ABSTRACT

Vehicular MIMO SAR Imaging in Multipath Environments

by

Li Li

Department of Electrical and Computer Engineering
Duke University

Date:_____

Approved:

_____
Jeffrey L. Krolik, Supervisor

_____
Loren W. Nolte

_____
Matthew S. Reynolds

An abstract of a thesis submitted in partial
fulfillment of the requirements for the degree
of Master of Science in the Department of
Electrical and Computer Engineering in the Graduate School
of Duke University

2011

Abstract

Current synthetic aperture radars (SAR) are most effective in simple, open terrains where direct-path propagation can be assumed. For ground-vehicle based SAR from a moving platform, however, strong multipath scattering off terrain features with the same direction of arrival and delays as direct path returns, results in serious imaging artifacts. Moreover, the dilemma between spatial coverage and azimuth resolutions and the along track sampling constraints are limiting factors which have thus far been precluded vehicular SAR in urban areas.

In this thesis, multi-input multi-output (MIMO) forward looking synthetic aperture radar is developed for imaging from a moving ground vehicle in urban multipath environments. MIMO methods are utilized to improve SAR images by suppressing directions of departure which would otherwise be multipath scattered and added to direct path returns by applying a three dimensional non-causal spatial filter in the direction-of-departure (DOD), direction-of-arrival (DOA), and Doppler-frequency domains which also enables the image with wide-swath and high resolution simultaneously. Both conventional and adaptive MIMO SAR methods are presented and compared in a multipath imaging simulation. The results suggest MIMO SAR offers substantial gains versus conventional SIMO imaging in presence of multipath.

Contents

List of Figures

Acknowledgements

I would like to thank my advisor, Dr. Jeffrey Krolik for his guidance and assistance over the last two years. I would also like to thank Dr. Loren Nolte and Dr. Matthew Reynolds for serving on my master's committee, and the numerous lab mates, Dr. William Lee, Jason Yu and Jonathan Odom, who have offered generous help of my graduate work at Duke. I would also like to thank the Office of Naval Research, for providing the funding for this research.

1. Introduction

Synthetic aperture radar (SAR) is a well-established remote sensing technique to obtain high resolution terrain map with a moving radar platform. Despite common SAR systems are generally based on airplanes or satellites, ground based SAR (GB-SAR) systems have drawn huge amount of attention to give high resolution images of the interested scene surrounding the vehicular platform which utilizes economic electronic and hardware equipment with narrow bandwidth of frequencies [1-6]. For example, automatic unmanned vehicle requires reliable cognitive imaging system to map the nearby man-made structures, such as walls, bridges or buildings; several ground penetrating radar (GPR) systems also employ the synthetic aperture idea to enhance the detection performance of underground objects [7, 8].

Principally, SAR provides high-resolution two-dimensional imaging by coherently sum the echoes received along the sensor platform trajectory. The azimuth, or along track resolution can be greatly enhanced by expanding the aperture size much longer than physical apertures. However based on the back scattering propagation model, the along tack sampling rate must be no greater than quarter of the minimum wavelength according to Nyquist sampling criteria to avoid azimuth aliasing [9, 10]. Conventional SAR can be divided into two types referring as Stripmap and Spotlight with the tradeoff between spatial coverage and cross-range resolutions [11]. A simple compromised mode as ScanSAR has been consequently developed, which provides a

wide imaging swath on the scarification of impaired azimuth resolution [12]. Even trough, simultaneously obtaining high resolution wide-swath SAR imaging is still dilemma to develop new imaging radar techniques. In addition, SAR is most effective in simple, open terrains where direct-path propagation can be assumed. For ground-vehicle based SAR from a moving platform, however, strong multipath scattering off terrain features, including street signs, parked vehicles, and the like, results in spread-Doppler clutter (SDC) which results in serious imaging artifacts. Vehicular SAR in urban areas, therefore, has thus far been precluded. In conventional SAR image formation, multipath scattering introduces false time of arrival and reflectivity imaging ghosts. Current multipath mitigation solutions for single channel SAR have been introduced by D. A. Garren [13] and W. Liang [14]. These approaches model the multipath echo as a direct path echo with a random phase offset.

In this work, a forward-looking (FL) multi-input multi-output ground (MIMO) SAR system is presented. The resulting FL-SAR configuration can resolve the left-right ambiguity of traditional side-looking mounted array, and achieve finer resolution in cross track direction, which is significant for vehicular wide-swath mapping systems. MIMO techniques, originally developed decades in wireless communications [15-17], utilizes a transmitting array, where each element radiates orthogonal waveform referring as transmission diversity, and also a receiving array for listening . By using a receiving array, as long as the inter-sensor spacing is no greater than half of the

wavelength, the azimuth aliasing problem can be mitigated, and the strict along track sampling criteria can be avoid [18]. Moreover, the transmitting diversity provides extra degree of freedom of transmitting, thus digital beamforming can be performed at the receiver side with respect to different transmitting angle, which enables the capacitance for high resolution and wide-swath imaging [27]. Meanwhile, potentials to mitigate multipath clutter is achieved by applying a three dimensional non-causal spatial filter in the direction-of-departure (DOD), direction-of-arrival (DOA), and Doppler-frequency domains as previously proposed for over-the-horizon radar in [19-21].

The organization of this thesis is as follows. Chapter 2 reviews the radar fundamentals including the range processing and azimuth processing, and the SAR concept is introduced in both intuitive and mathematic sense. Chapter 3 introduce the proposed FL MIMO ground-based SAR system by step by step interpreting in detail how it can fit the purpose of wide-swath high resolution terrain mapping by resolving the problems for the conventional SAR mentioned above. Several image reconstruction methods are derived and compared in Chapter 4 for the proposed system, and set of simulation evaluations are conducted in Chapter 5. Finally, conclusions are drawn in Chapter 6.

2. Synthetic Aperture Radar Basic

This chapter gives a brief review of the concept of SAR, including radar fundamentals, and how its data processing can be expressed with a physical and mathematical model. There are abundant books and reference about hardware, system and signal processing algorithm development of radar and SAR techniques. The radar fundamentals covered in this thesis is referred by Richards in detail given by [22]. Most of mathematic modes for SAR utilized in this work and signal processing are given by Soumekh in [23].

Section 2.1 gives a detail mathematical review of the Linear Frequency Modulated Continuous Waveform (LFM-CW) Radar technique, which enhance the range resolution with pulse compression, as well as introduction of the stretch processing technique which significantly reduces the cost of the radar receiver hardware design and discussion of sampling in fast time. Section 2.2 discusses the basic linear array theory which is essential for the concept of synthetic aperture. Section 2.3 introduces the synthetic aperture technique which resolves the cross range resolution by forming a virtual array in the long track direction of the SAR platform. Both stripmap and spotlight mode SAR will be introduced by comparing their own strengths and weaknesses. Practical imaging issue such as radar range cell migration problem and the three most common solutions will also be discussed in this section.

2.1 Radar Fundamentals with Range Processing

Radar (i.e., Range Detection and Ranging) works by transmitting pulses of electromagnetic energy, which are propagated at speed of light and bounced by the target surfaces producing return echoes that are received by the receiving antenna. For monostaitc radar (i.e., the transmitting and receiving antenna are collocated), the target slant range R can be determined from the measured time delay α of the two-way propagation of the echo by the equation

$$R = \frac{\alpha \cdot c}{2} \tag{2.1.1}$$

where c is the speed of light. Measuring the target ranges and the associated reflection intensity are the most conventional functions of the radar systems.

The radar resolution is defined as the minimal distance at which two close spaced discrete targets can be unambiguously separated. For conventional short pulsed radar, high range resolution can be achieved by utilized the shorter the pulse duringτ, which requires the lower the transmitted energy since the energy the instrument can emit in a finite timespan is limited. However, radar detection performance requires higher pulse energy with longer pulse during. Pulse compression waveforms, which decouple energy and resolution, are obtained by increasing the spectral bandwidth of the simple pulse with frequency or phase modulation, where the spectral width of the modulated pulse $B \approx \frac{1}{\tau}$. Therefore the pulse compressed range resolution ΔR, as a function of transmitting bandwidth is given as

$$\Delta R = \frac{\tau \cdot c}{2} \approx \frac{c}{2B} \tag{2.1.2}$$

where c is the speed of light, τ is compressed pulse duration and B is the transmitting bandwidth.

One most commonly utilized pulse compressed waveform is referred as the linear frequency modulated waveform. The ideal transmitted signal of a LFM waveform is a chirp with temporal frequency increasing linearly with the frequency modulation slope of $K_{FM} = B/\tau$, where B is the signal bandwidth in Hertz and τ the frequency sweeping duration in second. The ideal transmitting signal with linear frequency sweep with starting frequency f_0 in complex equivalent form can be written as:

$$s(t) = \exp\{j\theta(t)\} = \exp\{j(2\pi f_0\, t + \pi K_{FM} t^2)\} \quad 0 \le t \le \tau \tag{2.1.3}$$

The instantaneous frequency of $s(t)$ in (2.1.3) is the derivative of the phase function:

$$f(t) = \frac{1}{2\pi}\frac{d\theta(t)}{dt} = f_0 + K_{FM} t \qquad 0 \le t \le \tau \tag{2.1.4}$$

Typical LFM waveforms work with exceptionally wideband signal (e.g., on the order of hundreds of MHz to GHz), and common digital system are difficult to implement due to the high instantaneous bandwidth. Therefore stretch processing technique has been developed which is most appropriate to obtain high range resolution for shorting range radar processing. The return signal is a delayed version of transmitting FM chirp (2.1.4) with arrival delay α and attenuation A. The stretch processed dechirped signal is achieved by multiplying the return signal with the conjugate of transmitting replica, given as:

$$r(t) = A\exp\{j(2\pi f_0\,(t+\alpha) + \pi K_{FM}(t+\alpha)^2)\} \times \exp\{-j(2\pi f_0\, t + \pi K_{FM} t^2)\}$$

$$= A\exp\{j(2\pi\alpha K_{FM}\mathrm{t} + 2\pi f_0\alpha + \pi\alpha^2 K_{FM})\} \approx \exp\{j(2\pi\alpha K_{FM}\mathrm{t} + 2\pi f_0\alpha)\} \qquad (2.1.5)$$

where the approximation is taken since α^2 is on the order of squared nanosecond while K_{FM} is on the order of megahertz. Since the instantaneous frequency is proportional to the time as given in (2.1.4), the dechirped signal can be written as a function of instantaneous frequency

$$r(t) \xrightarrow{f_0 + K_{FM} t} r(f) = A\exp\{j2\pi\alpha f\} \qquad f_0 \le f \le f_0 + B \qquad (2.1.6)$$

Equation (2.1.1) can be thus viewed as the temporal frequency domain received data with delay information encoded in the phase at each frequency swept over the entire transmitting frequency band. A graph interpretation of this is given in Figure 1, where the relative delay is measured at each instantaneous frequency as time sweeping over the pulse during τ. Therefore, a time delay profile can be reconstructed by taking Fourier transform for (2.1.6) over f. The resulting 3-dB time delay resolution is then given as $1/B$, and the radar range resolution can be straightforwardly calculated as $c/2B$, which is equivalent as given in (2.1.2).

For conventional matched filter based radar receiver, the maximum unambiguous range is given by $cT_p/2$ where T_p is the pulse repetition interval. However, stretch processing as introduced earlier, is developed for short range radar processing, and the maximum ambiguous range in this case is limited by the sampling rate in the A/D converter. Denoting the sampling rate of the ADC as f_s samples per

second, the sampling interval in the instantaneous frequency (i.e., the frequency difference between each sampled frequency bins) can be written as $B/f_s\tau$. In this case, the maximum ambiguous delay is derived as $f_s\tau c/4B$.

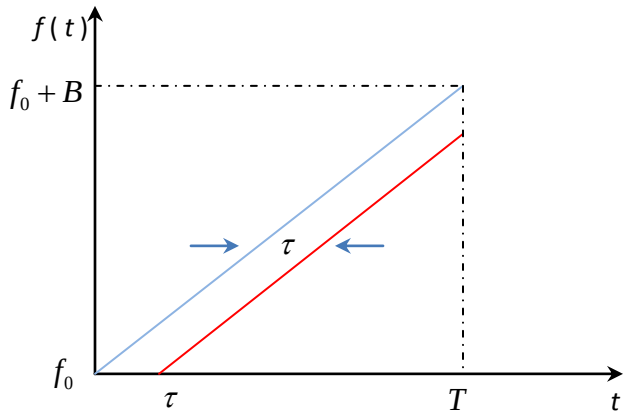

Figure 1: Stretch processing for LMF pulse compression waveform

2.2 Linear Array Theory

Before moving to the concept of SAR, we need to introduce the basic theory of array signal processing. In most array processing case, we are dealing with the uniform linear array (ULA) which has the array elements placed along a straight line with a uniform spacing *d*. In the 2-D scenario, assume the incident wave is a plane wave which is a sinusoid wave whose wavefronts (surfaces of constant phase) are infinite parallel planes perpendicular to the Poynting vector of the wave, shown in Figure 2, which can be written as 3-D complex exponential form as:

$$f(t,\mathbf{x}) = \exp\{j(\omega t - \mathbf{k}^T\mathbf{x})\} \qquad f_0 \le f \le f_0 + B \tag{2.2.1}$$

where $\mathbf{x} = [x\ y]^T$ and $\mathbf{k} = \left[k_x\ k_y\right]^T$ is wave number vector with the dispersion relationship:

$$k^2 = \frac{\omega^2}{c^2} = k_x^2 + k_y^2 = k^2 \sin\theta + k^2 \cos\theta \tag{2.2.2}$$

where θ is the azimuth angle in polar coordinates. Since the array element is uniformly placed along a straight line (i.e., $\mathbf{x}$ is unformly sampled and linearly increases), assume the phase center of the array is at the origin, then $x_i = \left(i - \frac{M}{2}\right)\Delta\mathbf{x}$, $i = 1, \ldots, M$, where M is the number of elements and $\Delta\mathbf{x} = [\delta x\ \ \delta y]^T$ is the inter-elemet incremence vector with $d = |\Delta\mathbf{x}|$. Thereby, we can express the wavefront of the planewave incident on an ULA as:

$$\exp\{-jk\left(-\frac{M}{2}\right)[\delta x \cdot \sin\theta + \delta y \cdot \cos\theta]\} \tag{2.2.3}$$

whose phase is linear as function of array index i.

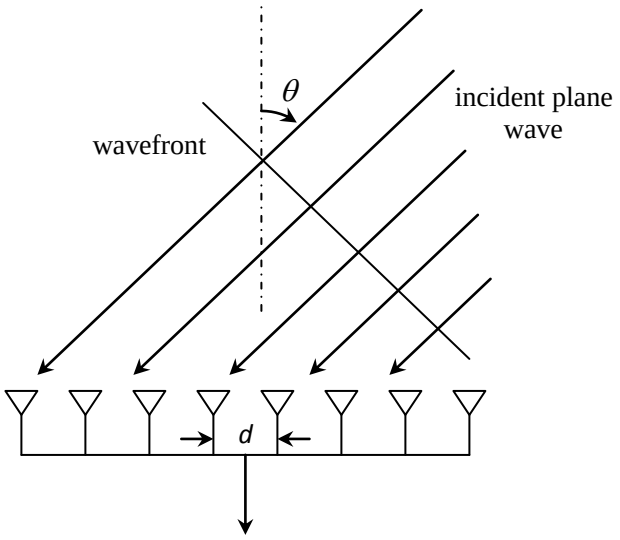

Figure 2: Uniform Linear Array with plane wave incident

Assume the array is placed as along the axis (i.e., $\Delta\mathbf{x} = [d\ 0]^T$), we can thus plot the array pattern as a function of k_x by taking the Discrete Time Fourier Transform (DTFT) respect to the element position, as shown in Figure 3, which can be written as

$$W(k_x) = \left|\frac{\sin M(d/2)k_x}{\sin(d/2)k_x}\right| \tag{2.2.4}$$

Given $k_x = k\sin\theta$, in order to force the visible region given in Figure 3 to achieve the entire bearing scan from $-\pi/2$ to $\pi/2$, the inter-element spacing d must no greater than the half wavelength to prevent the grating lobe. On the other hand, the Rayleigh resolution of k_x is inverse proportional to the aperture length, given by $1/L$ where $L = Md$ is the entire array length. Therefore, the angular resolution of $\sin\theta$ can be derived straightforwardly as λ/Md, which decreases as the frequency of incident wave increases given d and M.

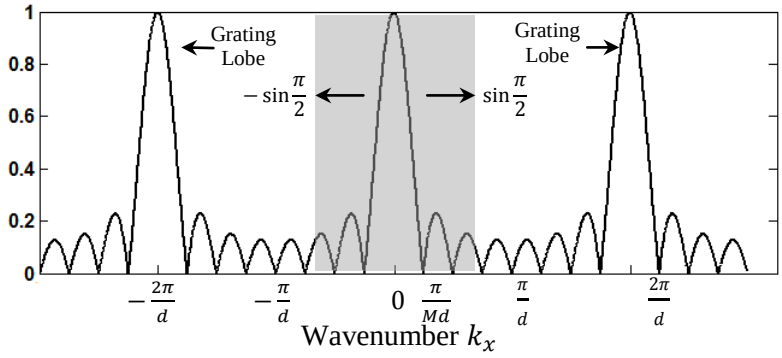

Figure 3: **Array pattern for an 8 elements ULA**

In the case of LFM plane wave whose phase is both linear in fast time domain and receiving element domain as given in (2.1.6) and (2.2.2), a range-bearing scan can be thus obtained by taking 2-D Discrete Fourier Transform, which can be transformed into

the XY coordinates efficiently. However, in many cases such as SAR, a near field situation is present in which case range dependent spherical wavefront is assumed, and the range cell migration problem is also considered where the targets do not stay in the same range bins across the sensor elements. Therefore, some nonlinear operations have to be considered in order to handle the near field effect, which will be introduced later in this work.

2.3 Synthetic Aperture Radar

For imaging purposes, using only the slant range measurement is not possible since objects with the same slant range cannot be separated with 1-D degree of freedom. In order to extend the observation space to 2-D, angular measurement can be obtained by using a receiver phased array using the classic array theory as introduced in the previous section. Real aperture imaging radars, which have been well established in the mid-twentieth century, use real antenna array to achieve high resolution. The resulting angular resolution is inverse proportional to the actual aperture length of the whole array. Instead of using a fixed receiver array which is costive and inflexible, SAR use moving platform, fast time and slow time data to synthesize a much large aperture, which is accomplished by displacing a single receiving antenna or a small size of array along the track parallel to the illuminated scene observing the same scene from by moving the platform with different position. A single image can be thus reconstructed or focused from the acquired offset range measurements from each “look”. The virtual

array formed thought the movement of radar platform is denoted as synthetic aperture or synthetic array, which gives the azimuth (cross-range) resolution:

$$\delta CR = \frac{\lambda R}{2L_{sar}} \tag{2.3.1}$$

where R is the range of interest and L_{sar} is the effective synthetic aperture length created by the movement of the platform with constant velocity v during total observation time T_{sar} $r$as:

$$L_{sar} = vT_{sar} \tag{2.3.2}$$

Two classic types of SAR are stripmap and spotlight SAR, as shown in Figure 4, by taking the tradeoff between azimuth resolution and illumination coverage. In the case of stripmap SAR, the physical antenna keeps the same transmitting pattern as the platform travels over the area of interest for imaging, so that the SAR is able to continually image strips of region as the platform travels by to form large area of coverage. However, as shown in the figure 4 (a), as the physical antenna pattern is fixed all the time, the efficient synthetic aperture length is also limited as a function of the antenna beamwidth, and the cross range is also limited as given in equation. In order to achieve higher resolution, spotlight SAR is introduced by steering the physical antenna beam towards the area of interest and continuously illuminates and imaging the region being mapped. In this case, the efficient aperture length is approximately equal to the actual distance the SAR platform travels, and the cross range resolution is thus significantly enhanced. In theory, the efficient aperture length for spotlight SAR can go

to infinity as long as the platform travelling, however, in practice, this aperture length is also limited by other factors such as propagation loss and maximum unambiguous range.

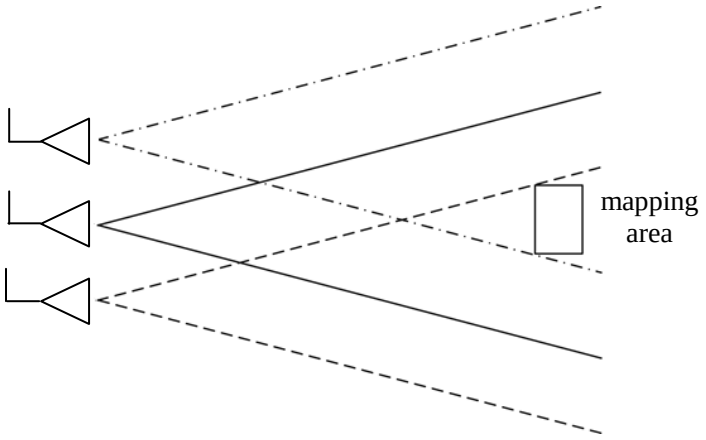

(a)

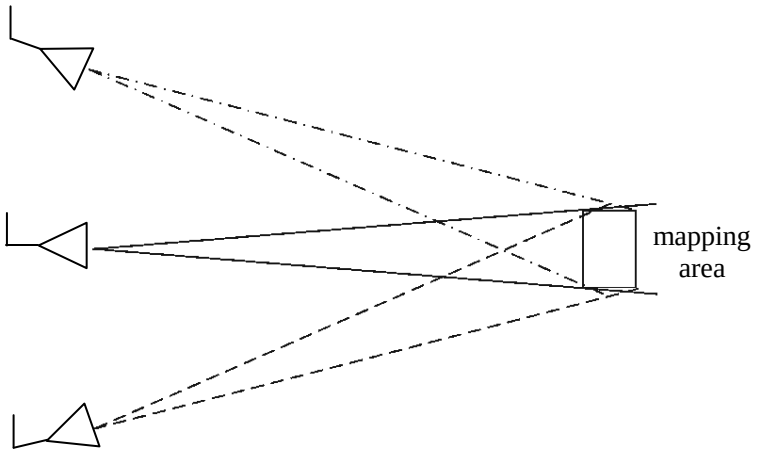

(b)

Figure 4: (a) Stripmap and (b) Spotlight SAR Geometry

2.4 SAR image reconstruction Algorithm Review

In this section, we will briefly review some common image reconstruction scheme for SAR in the literature. In Section 2.3, we have introduced the linear array theory by assuming the incoming signal is a planewave. However, in SAR scenario, since the effective aperture length can be long enough so that the imaging problem can be viewed as a near field processing, companying with the range cell migration issues as shown in Figure 5 with 3 discrete targets. Not that the curvature of these migrations are range dependent, therefore the corrections are non-trivial to perform.

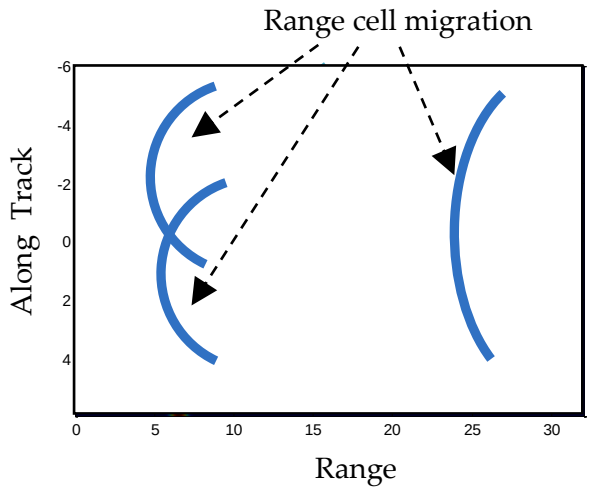

Figure 5: Illustration of Range Cell Migration problem for three discrete targets

Three most common used SAR processing algorithms for the range migration issue are range Doppler (RDA), chirp scaling algorithms (CSA) and the Omega-K algorithms [24, 25]. In The RDA performs with an azimuth frequency dependent secondary range compression and a range dependent range cell migration correction

which perform a coordinate transformation decoupling the range and across track variables. CSA is essentially similar as the RDA but uses the 3rd Taylor Series expansion to replace the interpolation step. Please note both RDA and CSA are approximation methods which discard higher order phase terms so that the range and cross range coupling cannot be completely compensated when the aperture is large enough or the illumination area is nearby. The frequency-wavenumber Omega-K algorithms perform the range cell migration problem through a frequency-wavenumber domain interpolation or coordinates transformation, referring as "Stolt mapping" [26], where no approximation is made in this approach. Therefore, to the purpose of wide-swath imaging, Omega-K algorithm is an appropriate solution for image reconstruction.

3. Vehicular SAR for Terrain Mapping

In this Chapter, instead of conventional airborne and satellite based SAR system; we are interested in a ground-based based imaging system or vehicular SAR as tools for terrain mapping such as traffic monitoring and obstacle objects detection. However, many practical problems have been considered for vehicular SAR imaging. For example, large coverage is expected for terrain mapping, however high azimuth resolution cannot be ignored for detecting small objects. Therefore, traditional stripmap and spotlight types of SAR are no longer suitable in this situation. On the other hand, 180° full swath scan is also expected for mapping the surrounding environment of the vehicular platform, and in this case, the azimuth undersampling/aliasing issue is present when the platform travels too fast and the along track sampling rate is larger than quarter of the wavelength of the transmitting signal. Moreover, for urban remote sensing, strong multipath returns scattering off terrain features, including street signs, parked vehicles, and the like, results in spread-Doppler clutter (SDC). Both of azimuth aliasing and multipath result in serious artifacts, which significantly degrade the imaging quality of the vehicle SAR.

This chapter brings the concept of the MIMO vehicle SAR trying to resolve the problems mentioned above. We are going to answer the questions as “why multi-input”, “why multi-output” and “how to make it work” intuitively and analytically. Moreover, the signal model will be given for imaging purposes.

3.1 Multiple Receiver SAR

The along-track sampling rate becomes a significant limitation of wide swath imaging for vehicle SAR. Assume a single omnidirectional receiving antenna is utilized, according to the Nyquist sampling theory, the true along-track sampling rate of any synthetic aperture system to obtain a 180° degree beamwidth [10] requires sampling no greater than quarter of the wavelength, i.e.,

$$\Delta u \leq \frac{\lambda}{4} \tag{3.1.1}$$

This azimuth sampling constraint requires either increasing in the pulse repetition frequency of the pulse train, which would degrade the detection performance, or reduce the platform travelling velocity. For example, assuming the transmitting frequency as 3 GHz, the along track sampling rate should be finer than 2.5 cm. Given pulse repetition interval as $0.01s$, the platform must travel no faster than 9 km/h, which is unrealistic in practice.

Instead of a single omnidirectional receiving antenna, multiple-receiver arrays can be viewed as a solution to this azimuth sampling issue [18]. SAR with multiple-receiver array, referring as "multi-output", offer a gain in the sampling rate equal to the number of receivers of the array, as long as the inter elements space is no greater than quarter wavelength. The sampling constrain can be rewritten by

$$\Delta u \leq \frac{\lambda N_r}{4} \tag{3.1.2}$$

where N_r is the number of receiving elements utilized. Therefore, the vehicular platform is able to travel N_r times faster than the using a single antenna, which proves wide swath imagery at realistic mapping rates.

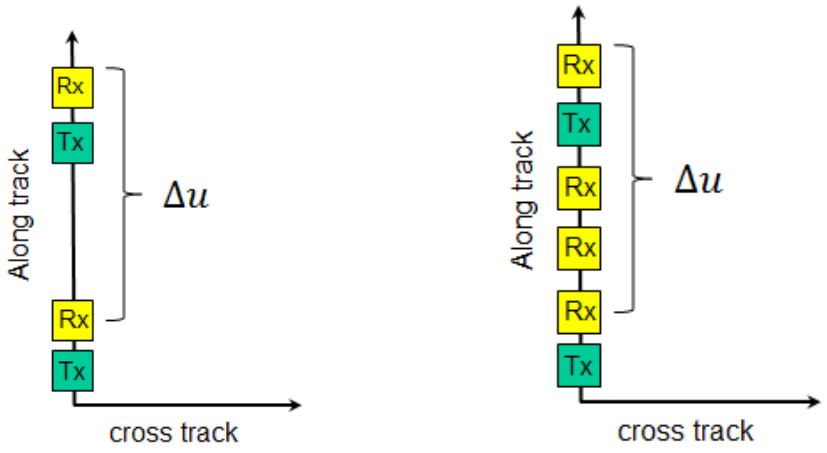

(a) (b)

Figure 6: (a) single receiver (b) multi-receiver

3.2 Transmitting Waveform Diversity

Stripmap SAR assumes fixed transmitting antenna pattern along track, which provides large coverage of area of interest, which is appropriate for terrain mapping. However, this is based on the scarification of reducing the efficient aperture length, or loss of azimuth resolution by utilizing the spotlight SAR. In order to achieve wide-swath with decent resolution, the feasibility of using multiple uncorrelated transmit waveforms to resolve ambiguity is brought into consideration, referred as Transmit Waveform Diversity (TWD), or "multi-input" waveform. The combination the TWD

with the multiple-receiver configuration introduced in the last section is termed as MIMO SAR [27].

TWD utilizes a transmitting antenna array, where each omnidirectional antenna element transmits uncorrelated signal. Non-casual transmitting beamforming can be performed at the receiver side to electronic steer the transmitting beam into the direction of interest. Therefore, the SAR is able to illuminate the whole area surrounding the platform since omnidirectional antenna is utilized. On the other hand, transmitting beamforming can focus a narrow beam on a specific area continuously as the platform travelling, which is equivalent as spotlight mode as shown in Figure 6. Hence, both large coverage and satisfactory resolution can be obtained based on TWD.

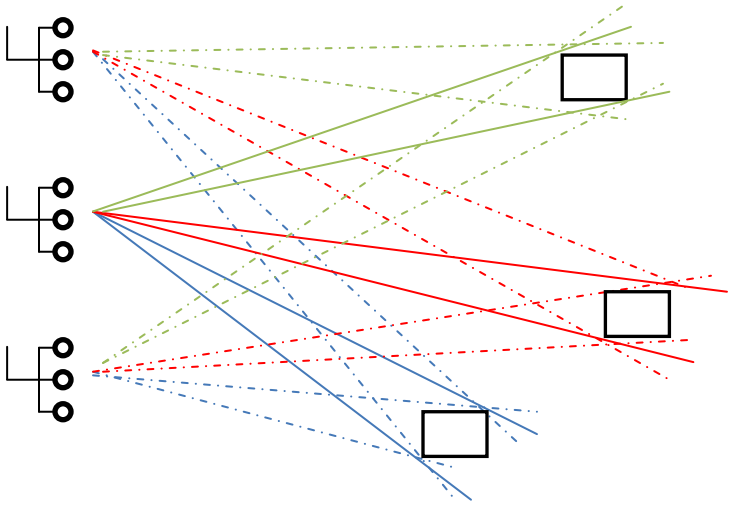

Figure 7: "Multi-input" SAR with transmitting diversity

The appropriate selection and generation of transmitted signals has been a contentious issue in the MIMO community. In much of the current literature, waveforms

radiated from each transmit element is assumed to be orthogonal, which, however, is not a requirement for MIMO radar. Three popular techniques to achieve orthogonality are to utilize time division, frequency division or code division multiplexing. However, the target or clutter scattering response is usually time-varying or frequency-selective, which results in potential performance degradation for the time and frequency division multiplexing, by incoherently extracting the information from the antenna correlation. Therefore, code division multiplexing waveform is commonly preferable in MIMO radar applications. Slow-time phase progression MIMO (SLO-MO) waveforms [19-21] encode different transmitting channels as Doppler shifts on conventional receivers without hardware changes, which, however, requires a multichannel arbitrary waveform generator, variable RF phase shifters, or using multiple carrier frequencies. Alternatively, double sideband and quadrature slow-time MIMO radar [28] provide an easy and inexpensive way to generate MIMO waveforms which have been used for decades in communications applications.

One well known limitation of the MIMO radar is the SNR loss compared to the traditional phased array radar with the factor of number of transmission elements. For the SAR case, this back draw can be compensated by increasing the observation time as the spotlight capacitance given by the MIMO transmission beamforming.

3.3 Multipath in SAR

Since conventional SAR are commonly airborne or space borne with narrow transmission beam, the multipath propagations are not a significant issue which limits the imaging performance. However, in the ground based SAR system, the surround multipath environment is much more complicated. Since we usually interest in wide-swath high resolution imaging, wide beam transmitter must be utilized. Therefore, the unmodeled multipath returns which from different direction of arrival than departure at the same range bins will result in image artifacts as shown in Figure 8 (a).

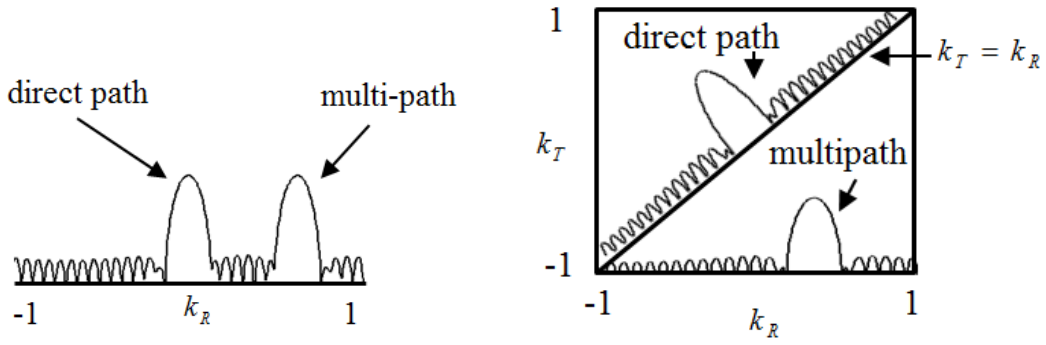

(a) (b)

Figure 8: Spatial spectrums at given range bins for (a) SIMO mono-directional case and (b) MIMO di-directional case

Given the extra degree of freedom of transmitting, we can performs a spatial filters which pass the direct path returns with DoA equal to DoD, and suppress the multipath returns with DoA different than DoD, as shown in Figure 8 (b). Therefore, the multipath artifact can be efficiently mitigated with the MIMO transmitting bemforming.

3.4 Forward Looking MIMO Vehicular SAR

In this work, we introduce a Forward Looking configuration MIMO SAR which can be mounted on a vehicular platform. Unlike the conventional side looking SAR, the forward looking structure places the transmitting and receiving array perpendicular to the platform trajectory. In this case, the left-right ambiguity can be resolved by electronically steering the receiving beam to the specific angle in both side of the platform, and the along track resolution can be also improved since the broadside of the array is along the platform path.

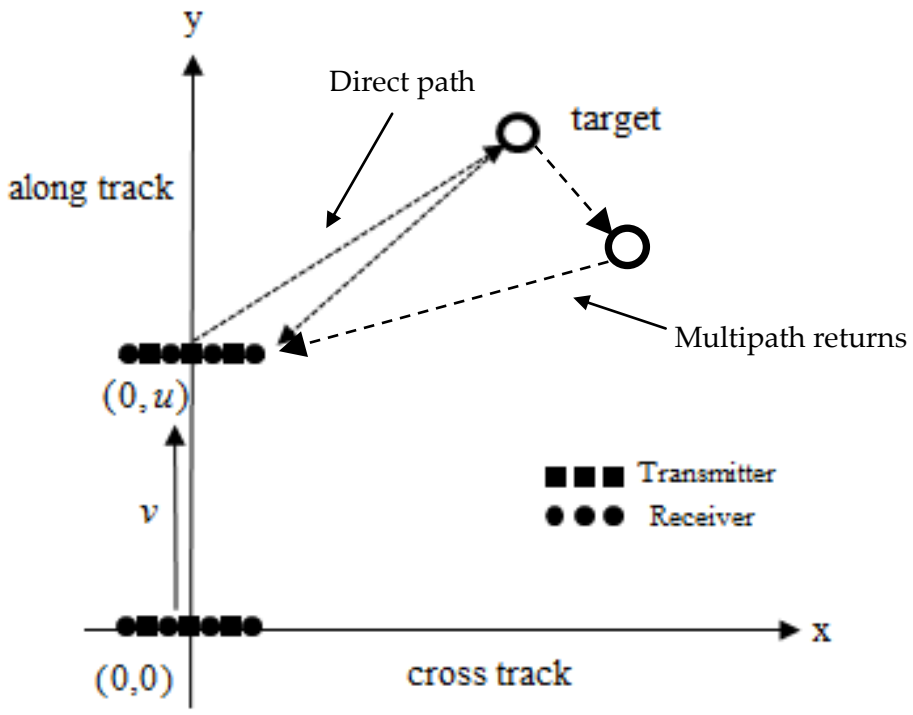

Figure 9: Transceiver geometry for the MIMO-FL SAR system

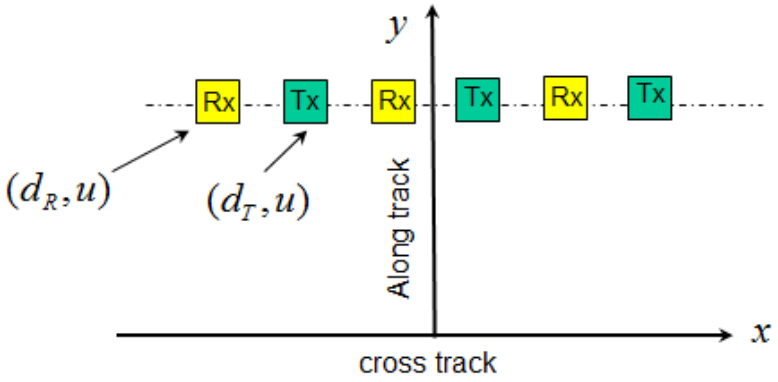

Figure 10: Geometry of the receiver and transmitter array

In addition, since k_x and k_y are quadrature based on the dispersion relationship, the along track sampling constraints (3.1.2) can be extended to the forward looking case directly. Figure 9 illustrate an example of such scenario in a 2D geometry which is appropriate for ground-based systems. Let the MIMO forward-looking platform travels along y axis, denoting the platform central position as (0, u). The transmitting and receiving antennas are mounted along the line $y = u$. Using the 2-D Green's function defined as:

$$g(x,y) = -\frac{j}{4}H_0^{(2)}(kr) \approx -\frac{1}{\sqrt{j8\pi k\rho}}\exp\{-jkr\} \tag{3.4.1}$$

where $H_0^{(2)}$ is a Hankel function of the 2nd kind [29], and the approximation is taken when the range ρ is much greater than the wavelength, the transmitting and receiving two way propagation ground return is given as:

$$y(\omega, d_T, d_R, u) = \iint f(x,y)H_0^{(2)}(kr_{tx})H_0^{(2)}(kr_{rx})\,dxdy \tag{3.4.2}$$

where $f(x, y)$ denotes the scattering reflectivity for focal point at coordinate (x, y) (we assume the reflectivity does not vary at different observation spot), d_T and d_R are the cross track coordinates of the transmitting and receiving elements respectively. As shown in Figure 8, the distance from transiting to focal point $r_{tx} = \sqrt{(x - d_T)^2 + (y - u)^2}$ and the distance from focal point (x, y) to receiving element $r_{rx} = \sqrt{(x - d_R)^2 + (y - u)^2}$. By given en r_{tx} and r_{rx} are much larger than the wavelength, equation (3.4.2) may be approximated as:

$$y(\omega, d_T, d_R, u) \cong \iint f(x, y) \frac{2}{\pi jk \sqrt{r_{tx} \cdot r_{rx}}} \exp\{-jk\,[r_{tx} + r_{rx}]\}\, dxdy \qquad (3.4.3)$$

The problem of interest for the image reconstruction of the FL-MIMO SAR proposed herein is to estimate the scattering reflectivity $f(x, y)$ for each point of interest by coherently combining the measurement data $y(\omega, d_T, d_R, u)$ at each temporal frequency step k, transmitting and receiving element d_T and d_R and from each observation position of the platform u.

4. Image Reconstruction for FL-MIMO SAR

In this Chapter, the image reconstruction algorithm for the proposed FL-MIMO SAR system will be discussed. As proposed in the last chapter, our goal is to accurately estimate the local reflectivity $f(x,y)$ at each point of interest. Assuming the number of sampled frequency bins as L, the number of transmitting/receiving elements as N_t/N_r and the number of along track observations as M, the 4D data in temporal frequency domain given in (3.4.3) can be obtained. Three kinds of image reconstruction methods in different domains will be introduced. The advantages and back draws of each method will be discussed in the text following.

4.1 Frequency-Space Domain Matched Filtering Imaging

An most straightforward image reconstruction algorithm is the conventional frequency space domain matched filtering imaging algorithm, or equivalently frequency space domain delay and sum method, by coherently sum all 4-D observed data described in (3.4.3) at each focal point of interest (x,y) for estimate the reflectivity $f(x,y)$ as:

$$\hat{f}(x,y) = \frac{1}{LMN_tN_r}\sum_{l=1}^{L}\sum_{i=1}^{N_t}\sum_{j=1}^{N_r}\sum_{l=1}^{L} w_{l,i,j,m}\, y\big(\omega_l, d_{T,i}, d_{R,j}, u_m\big)\exp\{jk\,[r_{tx}+r_{rx}]\} \quad (4.1.1)$$

where w denote the window function for each dimension. By using the vector notation we can write (3.1.1) in the form as:

$$\hat{f}(x,y) = |\overline{\mathbf{e}}(x,y)^H\overline{\mathbf{y}}| \quad (4.1.2)$$

where H denotes conjugate transpose, $\bar{\mathbf{y}}$ is the LN_tN_rM by 1 data vector which stack the 4-D data into one dimensional vector and $\bar{\mathbf{e}}(x, y)$ is the steering vector at given focal position (x, y).

The frequency space domain matched filtering imaging algorithm provides exact estimation modeling in find the reflectivity. However, it is very computational inefficient way since the inner product operation has to be performed at each focal point and the vector dimension LN_tN_rM can be a very large number which is usually greater than1000. Therefore, this delay and sum data independent method is not practically efficient image algorithm for large swath mapping. However, if only a small portion area is interest, this method can be also appreciable since it utilizes the exact data model without any approximations.

4.2 Frequency-Wavenumber Domain Imaging with SIMO equivalence

Since wide-swath mapping is considered, a frequency wavenumber domain formation of image is brought into states. The frequency wavenumber domain can be interpreted as Fast Fourier Transform (FFT) based approach, which is known as the Omega-K algorithm. This algorithm estimate a 2D spectral in k_x and k_y domain with nonlinear coordinate transform referring as Stolt Mapping, and obtain the reflectivity map $f(x, y)$ through a 2D inverse FFT, which is computational efficient for large map imaging.

Starting from the temporal frequency domain received signal (3.4.3), the two way bistatic range $r_{tx} + r_{rx}$ can be approximated based on Taylor approximation as:

$$F(x) + F(x+\epsilon) \approx 2F\left(x + \frac{\epsilon}{2}\right) + \frac{\epsilon^2}{4}F''\left(x + \frac{\epsilon}{2}\right) \tag{4.2.1}$$

for $x \gg \epsilon$. Therefore, for any focal point (x, y) where x is much larger than the actual array length, we can have:

$$r_{tx} + r_{rx} \approx 2\sqrt{(x - 0.5(d_R + d_T))^2 + (y-u)^2} \tag{4.2.2}$$

Hereby, ignoring the amplitude term (3.4.3) can be approximated as:

$$y(\omega, d_T, d_R, u) \cong \iint f(x,y)\exp\{-j2\frac{\omega}{c}\left[\sqrt{(x - 0.5(d_T + d_R))^2 + (y-u)^2}\right]\}dxdy \tag{4.2.3}$$

referring as phase center approximation [31]. Let $d = 0.5(d_R + d_T)$, and then:

$$y(\omega, d, u) = \iint f(x,y)\exp\{-j2\frac{\omega}{c}\left[\sqrt{(x-d)^2 + (y-u)^2}\right]\}dxdy \tag{4.2.4}$$

The mapping from (4.2.3) to (4.2.4) is a dimension reduction transform. By combining different d_R and d_T pairs which have same values of d (for example, the pairs$d_R = 0.1$, $d_T = -0.1$ and $d_R = 0.2$, $d_T = -0.2$ share the same value $d = 0$), the MIMO data string can be mapped into a SIMO equivalence form. Taking the Fourier transform in d domain on (4.2.5) using the method of stationary phase approximation [30] (the detail derivation is given in Appendix A), and letting $k = \frac{\omega}{c}$, we obtain:

$$\begin{aligned} Y(k, k_d, u) &\cong \iint f(x,y)\exp\left\{-jk_d x - j\sqrt{4k^2 - {k_d}^2}(y-u)\right\}dxdy \\ &= \exp\left\{j\sqrt{4k^2 - {k_d}^2}u\right\}\iint f(x,y)\exp\{-jk_d x - j\sqrt{4k^2 - {k_d}^2}y\}dxdy \end{aligned} \tag{4.2.5}$$

From (4.2.5), it can be seen that there is a phase shift between each slow-time or along track sample at spatial frequency $\sqrt{4k^2 - {k_d}^2}$. A 2-D spectrum $Y(k, k_d)$ can be thus obtained by coherently summating each slow-time samples in u domain as:

$$\hat{Y}(k, k_d) = \sum_u Y(k, k_d, u) W_u(k, k_d) \tag{4.2.6}$$

where

$$W_u(k, k_d) = \exp\{-j\sqrt{4k^2 - {k_d}^2}u\} \quad \text{for positive frequency}$$

or

$$W_u(k, k_d) = \exp\{j\sqrt{4k^2 - {k_d}^2}u\} \quad \text{for negative frequency}$$

At this point, a Fourier domain change of variable is given by:

$$k_y = \sqrt{4k^2 - {k_d}^2}$$

$$k_x = k_d$$

and $$\widehat{F}(k_x, k_y) = S\{\hat{Y}(k, k_d)\}$$

where $S\{\cdot\}$ refers to the coordinate transform which is performed via a frequency domain interpolation, known as Stolt mapping [26]. Thus, the 2-D reflectivity image $f(x, y)$ can be obtained through a 2-D inverse Fourier Transform in both k_x and k_y.

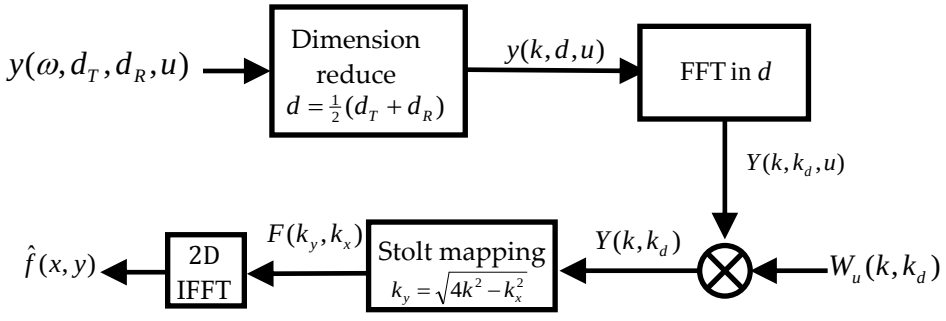

Figure 11: Processing diagram for imaging with SIMO equivalence form

4.3 Space-Time Imaging in Frequency-Wavenumber Domain

This section focuses on relating the MIMO SAR image reconstruction algorithm with the traditional STAP method. For traditional or far-field STAP, narrowband signals are usually assumed (i.e., $k = \omega/c$ is a constant), and the STAP weights are applied to each range gate independently in time domain. It also assumes that the targets stay in the same range bin, and the phase shifts in both slow-time and spatial frequency domains are linear. Letting N_t, $N_r$and M represent numbers of samples in the transmitting, receiving and slow-time domains, respectively, the direct-path backscatter wavefront vector ($\phi_T = \phi_R$), with transmitting/receiving angle ϕ and Doppler frequency f_D, is expressed as

$$\mathbf{e}(\phi, f_D) = \mathbf{a}_T(\phi) \otimes \mathbf{a}_T(\phi) \otimes \mathbf{b}(f_D)$$

where $$\mathbf{a}_T(\phi) = \left[\exp\{jkd_{T.0}sin\phi\}, \ldots \exp\{jkd_{T.N_t-1}sin\phi\}\right]^T$$

$$\mathbf{a}_R(\phi) = \left[\exp\{jkd_{R.0}sin\phi\}, \ldots \exp\{jkd_{R.N_r-1}sin\phi\}\right]^T$$

$$\mathbf{b}(f_D) = \left[\exp\left\{j2\pi f_D \frac{u_0}{v}\right\}, \ldots \exp\left\{j2\pi f_D \frac{u_{M-1}}{v}\right\}\right]^T$$

Here v denotes the platform velocity, and the Doppler frequency for direct- path clutter

$f_D = \frac{2v}{\lambda} sin\phi$ for side-looking array

or

$f_D = \frac{2v}{\lambda} cos\phi$ for forward-looking array

However, a wideband near-field scenario is often considered in SAR signal processing, especially in the slow-time domain (the synthetic aperture length is long, and the target

is no longer in the same range bin in slow time, commonly called range walk). Therefore, modifications of the far-field STAP algorithm have to be made in order to be used for SAR image reconstruction.

Firstly, due to the wide swath and wideband system characteristics and the presence of range walk, STAP in the frequency and wavenumber domain is used instead of time domain. Starting with the temporal frequency domain received signal (1), take the Fourier transforms in both d_T and d_R without the phase-center approximation introduced in the previous, obtaining:

$$
\begin{aligned}
&Y(k, k_T, k_R, u) \\
&= \iint f(x,y) \exp\left\{-j(k_T + k_R)x - j\left(\sqrt{k^2 - {k_T}^2} + \sqrt{k^2 - {k_R}^2}\right)(y-u)\right\} dxdy \\
&= \exp\left\{j\left(\sqrt{k^2 - {k_T}^2} + \sqrt{k^2 - {k_R}^2}\right)u\right\} \iint f(x,y) \exp\left\{-j(k_T + k_R)x \right. \\
&\qquad \left. - j\left(\sqrt{k^2 - {k_T}^2} + \sqrt{k^2 - {k_R}^2}\right)y\right\} dxdy \\
&= \exp\left\{j\left(\sqrt{k^2 - {k_T}^2} + \sqrt{k^2 - {k_R}^2}\right)u\right\} Y(k, k_T, k_R | u) \qquad (4.3.1)
\end{aligned}
$$

Note that, the first term of equation (4.3.1) is the slow time phase shift in MIMO SAR (equation (4.3.1) can be also obtained by solving the wave equation as in [7]). In the case of direct path echo, the transmitting angle and the receiving angle are identical, i.e.

$$k_x = 2k_T = 2k_R \qquad (4.3.2)$$

and equation (4.3.1) becomes:

$$Y(k, k_x, u) = \exp\left\{j\sqrt{4k^2 - {k_x}^2}u\right\} Y_u(k, k_x) \tag{4.3.3}$$

One can compare the slow-time term in (4.3.3) with the far-field Doppler frequency of FL-SAR system:

$$f_d = \frac{2u}{\lambda} cos\theta = \frac{k_y}{2\pi} = \frac{\sqrt{4k^2 - {k_x}^2}}{2\pi} \tag{4.3.4}$$

Assuming far-field propagation among the transmitting and receiving elements at one slow-time sample, with the relationship in (4.3.2), the direct-path clutter return in temporal frequency domain is proportional to:

$$\exp\{-jk_x d_T/2\}\exp\{-jk_x d_R/2\}\exp\left\{j\sqrt{4k^2 - {k_x}^2}u\right\} \tag{4.3.5}$$

These processed signals can be gathered into a wavefront vector at k and k_x

$$\mathbf{e}(k, k_x) = \mathbf{a}_T(k_x) \otimes \mathbf{a}_R(k_x) \otimes \mathbf{b}(k, k_x) \tag{4.3.6}$$

where

$$\mathbf{a}_T(k_x) = [\exp\{jk_x d_{T.0}/2\}, \ldots \exp\{jk_x d_{T.N-1}/2\}]^T$$

$$\mathbf{a}_R(k_x) = [\exp\{jk_x d_{R.0}/2\}, \quad \ldots \exp\{jk_x d_{R.M-1}/2\}]^T$$

$$\mathbf{b}(k, k_x) = \left[\exp\left\{j\sqrt{4k^2 - {k_x}^2}u_0\right\}, \ldots \exp\left\{j\sqrt{4k^2 - {k_x}^2}u_{L-1}\right\}\right]^T$$

Thus, a 2-D spectrum matrix $\hat{Y}(k, k_x)$ can be obtained by applying the steering vector (10) to the NML by 1 observation vector at different frequency bins, as

$$\hat{Y}(k, k_x) = \mathbf{e}(k, k_x)^H \mathbf{y}(k) \tag{4.3.6}$$

where $\bar{\mathbf{y}}(k)$ is the $N_t N_r M$ by 1 data vector which stack the 3-D data at wavenumber k into one dimensional vector. Finally, the Stolt mapping is applied as in the previous section by transforming $Y(k, k_x)$ into $F(k_x, k_y)$, and 2-D reflectivity map is obtained.

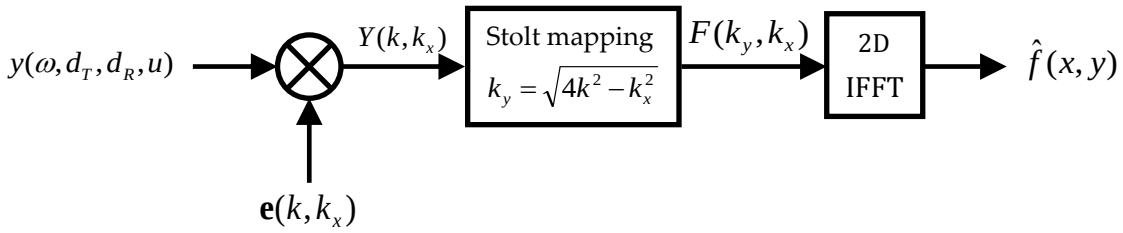

Figure 12: Processing diagram for imaging based on 3D space-time steering vector

In order to maximize the SINR in presence of strong multipath clutter and moving targets, adaptive STAP weights can be used instead of conventional weights (10). For example, the well-known minimum variance distortionless response (MVDR) filter can be expressed as following optimization problem:

$$\min_{\mathbf{w}} \mathbf{w}(k, k_x)^H \mathbf{R}_{\text{dcf}}(k)^{-1} \mathbf{w}(k, k_x) \tag{4.3.6}$$

$$\text{subject to} \qquad \mathbf{w}(k, k_x)^H \mathbf{e}(k, k_x) = 1$$

where $\mathbf{R}_{\text{dcf}}(k)$is $N_t N_r M$ by $N_t N_r M$ direct path clutter free variance matrix. The solution to the optimization problem stated above is

$$\mathbf{w}(k, k_x) = \frac{\mathbf{R}_{\text{dcf}(k)}{}^{-1} \mathbf{e}(k, k_x)}{\mathbf{e}(k, k_x)^H \mathbf{R}_{\text{dcf}(k)}{}^{-1} \mathbf{e}(k, k_x)} \tag{4.3.6}$$

Since practically it is hard to accurately estimate $\mathbf{R}_{\text{dcf}}(k)$, the total covariance matrix $\mathbf{R}_{\mathbf{yy}}(k)$ is chosen instead of $\mathbf{R}_{\text{dcf}}(k)$ **,** with proper diagonal loading for robustness of steering mismatch. This refers to the minimum power distortionless response (MPDR)

[32]. One limitation of the MVDR/MPDR solution is that they are optimized with respect to minimize the power of undesired signal, however the 2D estimated spectrum $\hat{Y}(k, k_x)$ are complex with both amplitude and phase. Hence, using the MVDR/MPDR criteria may cause phase distortions of the estimated $\hat{Y}(k, k_x)$ which results in perturbed image estimates $\hat{f}(x, y)$. On the other hand, due to the high complexity of the inversion of such a large covariance matrix, partially or reduced-rank adaptive techniques will be studied in the future work.

5. Simulation

In order to illustrate performance of the proposed Forward-Looking MIMO SAR system, evaluations are presented based on simulated data for a vehicular radar system. This simulation allows for a controlled analysis with exact knowledge of the environmental layout and multipath scenario. In order to represent realistic radar signals, the simulation setup is based on realistic parameters which are utilized by the STARDAR indoor FMCW MIMO radar system developed at Duke University [33, 34].

Table 1: List of simulation parameters.

RF bandwidth	2.1 – 2.7GHz
Tx position (d_T):	-0.075: 0.025: 0.075 m
Rx position (d_R): -	-0.175: 0.025: 0.175 m
Platform velocity(v):	10 m/s
PRI:	0.02 s
Along track Δu:	0.2 m
Synthetic Aperture length:	5 m

Consider a MIMO FL-SAR system which is working within the 600 MHz RF frequency band from 2.1GHz to 2.7 GHz with 8 transmitting antenna and 16 receiving antenna which are mounted parallel with x-axis and perpendicular to the platform trajectory. The inter-element spacing is 5 cm, smaller than half of the minimum

wavelength. The platform travels along the y-axis with a constant velocity 10 m/s. The pulse repeated interval is assumed as 0.02 s, with the corresponding along track sampling rate as 0.2 m. The total observation time is 2.5 s, which is equivalent to a 5 m synthetic aperture length. The detail parameters used are listed in Table.1.

In the simulation, we only interest in the multipath rejection by utilized the transmitting beamforming given by MIMO structure. Therefore, we compare two different configurations: MIMO version as proposed in this thesis and SIMO version which utilizes a single omnidirectional antenna for transmitting. Since the gain issue between MIMO and SIMO are not considered here, a totally noise free scenario is assumed in most of the simulation setups. We also want to exam the multipath mitigation with different power level of multipath, therefore, the total input direct-path to multipath ratio (DMR) is defined as the energy of direct path returns divides that of the multipath returns. The lower the DMR, the stronger the multipath returns are present.

The first phase of simulation is to image six spread stationary point targets locate in the x-y plane, each of which has a unit reflectivity. The location of each point target is given by (3, 4), (5, 4), (3, 9), (5, 9), (3, 13) and (5, 13). A first-order scattering model between these 6 targets is used, which results in a total of 30 multipath returns. In the first run, the DMR is set to be 0 dB. Both of the SIMO and MIMO configuration of the SAR systems are studied here, and image reconstruction algorithm is based the

conventional weights shown in (4.3.6). The results of the simulation are shown in Figure 13. In the SIMO case, Figure 13 (a), all of the 6 targets are focused without spatial aliasing due to utilization of the array; however, the image quality is perturbed by the multipath ghosts on the edge of the image. In the MIMO case, Figure 13 (b), the multipath ghosts are successfully mitigated, and the peak value of the strongest ghost is reduced by -14 dB.

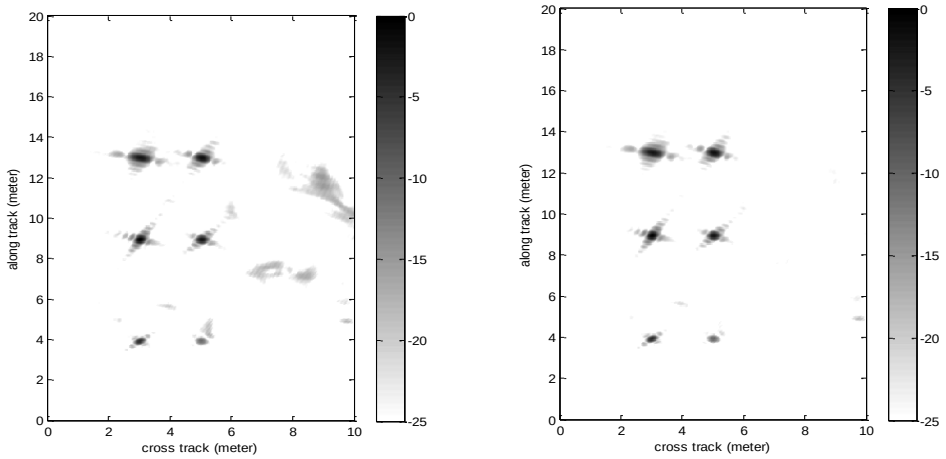

(a) (b)

Figure 13: Simulation result in presence of weak mutipath for (a) SIMO case and (b) MIMO case

A second phase of simulation experiment is in presence of strong multipath clutters by setting the input MDR at -10 dB. Since the multipath returns are relatively strong, SIMO configuration is not considered here. Therefore, both conventional MIMO STAP weights and MPDR weights are compared in this phase, shown in Figure 14. It can be observed that, perturbed by the strong multipath clutters, the conventional imaging result is poor due to the high sidelobes in Figure 14 (a). By using the adaptive weights as

in Figure 14 (b), the sidelobes and clutters are efficiently mitigated, and all the six stationary point targets can be identified.

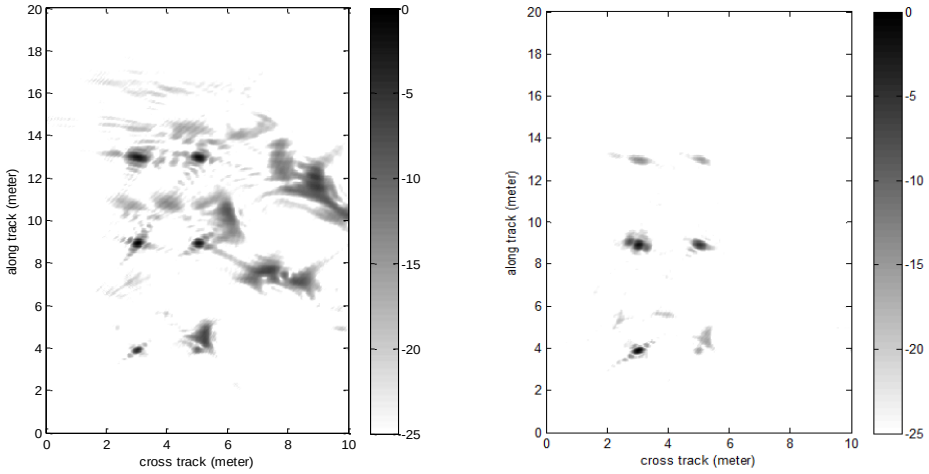

(a) (b)

Figure 14: Simulation result in presence of strong mutipath by using (a) conventioanl MIMO weights and (b) MPDR MIMO weights

A more complicated image is considered in the third phase of simulation. A room with three cylinders is tested as an input image in Figure 15 (c). We assume all the walls and objects, solid lines in Figure 15 (c), are visible without geometric modeling. However, the multipath returns are modeled according to geometric optics. The total input direct-path to multipath ratio is setting as 0 dB and only conventional weights are used. The results are illustrated in Figure 15 (a) and (b), and similar to the previous experiments, the MIMO image exhibits robustness to the multipath returns. However, since only 4 transmitting elements are used, multipath returns inside the mailobe region are still visible.

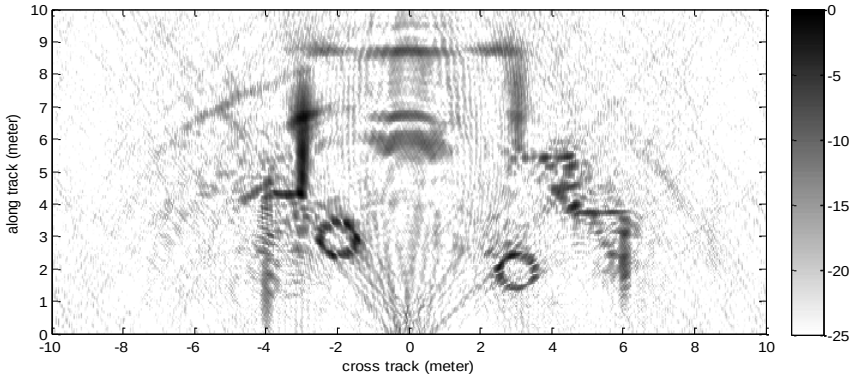

(a)

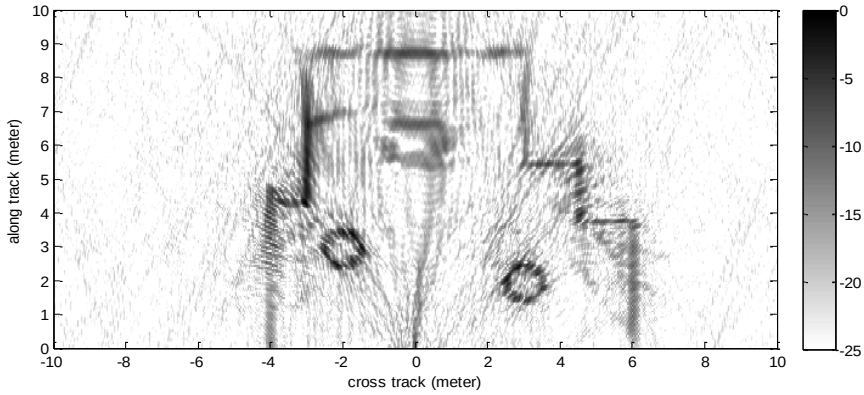

(b)

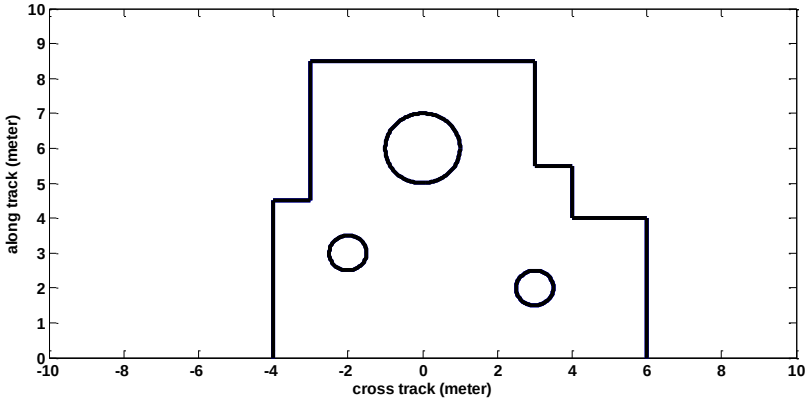

(c)

Figure 15: Simulation result for a room image by using (a) conventional SIMO weights and (b) conventional MIMO weights, with ground truth (c)

6. Conclusions and Future Work

The concepts and results proposed in this work illustrate the feasibility of the novel forward-looking multi-input multi-output vehicular SAR for terrain mapping. Image reconstruction algorithms in frequency-space domain and in frequency-wavenumber domain are reviewed and modified into the MIMO transceiver configuration. The frequency-space domain imaging formation algorithm introduced in Section 4.1, which utilizes the exact data model, is a straightforward but computational inefficient method and thus is only appropriate for small area mapping. The frequency-space domain method is a Fourier analysis based method. We introduced two general methods. One uses Taylor Series expansion, or phase-center approximation, to approximate the MIMO problem into an SIMO equivalent form, which is efficient but has poor multipath rejection. The exact MIMO formation algorithm has been derived in Section 4.3 which performs a 3-D non-causal filtering, (conventional or adaptive) in transmission, receiving and slow time domain, and the multipath clutter echoes are successfully mitigated by the proposed MIMO processing algorithm as shown in the simulation results in Chapter 5.

Future studies include the estimation of direct-path backscatter free covariance matrix from the received data to achieve robust beamforming output and use of a reduced-rank adaptive filter to increase computational efficiency. Also, the performance of the algorithm will be evaluated by using a real MIMO radar data from STRADAR

indoor S-band FMCW testbed radar [33-34]. Several practical problems will be considered such as autofocus when the plat form trajectory is not a perfect straight line, so that the exact platform positions are unknown at each look. Different geometries of the array configurations and hardware issues such as transmission frequency and antenna selections are also significant to obtain decent image.

Appendix A

This appendix provides the full derivation of Fourier transform of equation (4.2.4) with respect to the sensor offset d based on the stationary phase approximation, to obtain the expression given in (4.2.5). Since the integrations with respect to x and y are linear operation, we can equivalently start from the response at an arbitrary point scatter at (x_0, y_0) with $f(x_0, y_0) = 1$, as

$$\tilde{y}(\omega, d, u) = \exp\{-j2k\,[\sqrt{(x_0 - d)^2 + (y_0 - u)^2}]\} \tag{A.1}$$

The Fourier Transform of $\tilde{y}(\omega, d, u)$ with respect to d is given as:

$$\begin{aligned}\tilde{Y}(\omega, K_d, u) &= \int \exp\left\{-j2k\left[\sqrt{(x_0 - d)^2 + (y_0 - u)^2}\right]\right\} \exp\{-jk_d d\}\, dd \\ &= \int \exp\left\{-j2k\left[\sqrt{(x_0 - d)^2 + (y_0 - u)^2}\right] - jk_d d\right\} dd \\ &\approx \exp\left\{-j2k\left[\sqrt{(x_0 - d')^2 + (y_0 - u)^2}\right] - jk_d d'\right\}\end{aligned} \tag{A.2}$$

where the stationary point, d', is found by solving

$$\frac{\partial}{\partial d}\left\{2k\left[\sqrt{(x_0 - d)^2 + (y_0 - u)^2}\right] + k_d d\right\} = 0 \tag{A.3}$$

which yields the solution given by:

$$d' = -\frac{k_d(y_0 - u)}{\sqrt{4k^2 - k_d^2}} + x_0 \tag{A.4}$$

Plug (A.4) back into (A.2), giving:

$$\tilde{Y}(\omega, K_d, u) = \exp\left\{-j2k\left[\sqrt{\left(\frac{k_d(y_0 - u)}{\sqrt{4k^2 - k_d^2}}\right)^2 + (y_0 - u)^2}\right] - jk_d\left(-\frac{k_d(y_0 - u)}{\sqrt{4k^2 - k_d^2}} + x_0\right)\right\}$$

$$= \exp\left\{-j\frac{4k^2(y_0-u)}{\sqrt{4k^2-k_d^2}} + j\frac{k_d^2(y_0-u)}{\sqrt{4k^2-k_d^2}} - jk_d x_0\right\}$$

$$= \exp\left\{-j\sqrt{4k^2-k_d^2}(y_0-u) - jk_d x_0\right\} \quad \text{(A.5)}$$

Therefore, by extending the single point scattering response (A.5) to the continuous scattering case, we can obtain the same expression as

$$Y(k,k_d,u) \cong \iint f(x,y)\exp\left\{-jk_d x - j\sqrt{4k^2-{k_d}^2}(y-u)\right\}dxdy$$

References

[1] Bennett, J.C.; Morrison, K.; , "Development of a ground-based, polarimetric synthetic aperture radar," *Aerospace Applications Conference, 1996. Proceedings., 1996 IEEE* , vol.4, no., pp.139-146 vol.4, 3-10 Feb 1996

[2] Bennett, J.C.; Morrison, K.; Race, A.M.; Cookmartin, G.; Quegan, S.; , "The UK NERC fully portable polarimetric ground-based synthetic aperture radar (GB-SAR)," *Geoscience and Remote Sensing Symposium, 2000. Proceedings. IGARSS 2000. IEEE 2000 International* , vol.5, no., pp.2313-2315 vol.5, 2000

[3] Yigit, Enes; Unal, Atilla; Kaya, Adem; Demirci, Sevket; Cetinkaya, Harun; Ozdemir, Caner; Vertiy, Alexey; , "Millimeter-wave ground based synthetic aperture radar measurements," *General Assembly and Scientific Symposium, 2011 XXXth URSI* , vol., no., pp.1-4, 13-20 Aug. 2011

[4] Morrison, K.; Bennett, J.C.; , "Development of a high-resolution ground-based synthetic aperture radar," *Geoscience and Remote Sensing Symposium, 1996. IGARSS '96. 'Remote Sensing for a Sustainable Future.', International* , vol.4, no., pp.2344-2346 vol.4, 27-31 May 1996

[5] Tarchi, D.; Lukin, K.; Leva, D.; Fortuni, J.; Mogila, A.; Vyplavin, P.; Sieber, A.; , "Implementation of Noise Radar Technology in Ground Based SAR for Short Range Applications," *Physics and Engineering of Microwaves, Millimeter and Submillimeter Waves and Workshop on Terahertz Technologies, 2007. MSMW '07. The Sixth International Kharkov Symposium on* , vol.1, no., pp.442-444, 25-30 June 2007

[6] Qi Yao-long; Tan Wei-xian; Xia Dong-kun; Wang Yan-ping; Hong Wen; , "Research on the near range imaging of Ground-based SAR system," *Synthetic Aperture Radar, 2009. APSAR 2009. 2nd Asian-Pacific Conference on* , vol., no., pp.455-458, 26-30 Oct. 2009

[7] Gu, K.; Wang, G.; Li, J.; , "Migration based SAR imaging for ground penetrating radar systems," *Radar, Sonar and Navigation, IEE Proceedings* - , vol.151, no.5, pp. 317- 325, 10 Oct. 2004

[8] Kabourek, V.; Černý, P.; , "SAR and Stolt Migration processing for plastic landmine detection," *Radioelektronika (RADIOELEKTRONIKA), 2010 20th International Conference* , vol., no., pp.1-4, 19-21 April 2010

[9] Tomiyasu, K.; , "Tutorial review of synthetic-aperture radar (SAR) with applications to imaging of the ocean surface," *Proceedings of the IEEE* , vol.66, no.5, pp. 563- 583, May 1978

[10] Rolt, K.D.; Schmidt, H.; , "Azimuthal ambiguities in synthetic aperture sonar and synthetic aperture radar imagery," *Oceanic Engineering, IEEE Journal of* , vol.17, no.1, pp.73-79, Jan 1992

[11] Freeman, A.; Johnson, W.T.K.; Huneycutt, B.; Jordan, R.; Hensley, S.; Siqueira, P.; Curlander, J.; , "The "Myth" of the minimum SAR antenna area constraint ," *Geoscience and Remote Sensing, IEEE Transactions on* , vol.38, no.1, pp.320-324, Jan 2000

[12] Moore, R.K.; Claassen, J.P.; Lin, Y.H.; , "Scanning Spaceborne Synthetic Aperture Radar with Integrated Radiometer," *Aerospace and Electronic Systems, IEEE Transactions on* , vol.AES-17, no.3, pp.410-421, May 1981

[13] D. A. Garren, J. S. Goldstein, D. R. Obuchon et al., SAR Image Formation Algorithm with Multipath Reflectivity Estimation, Proc. Of IEEE Radar Conference 2004, 2004, pp.323-328.

[14] Wang Liang; Huang Xiaotao; Zhou Zhimin; Song Qian; "Research on UWB SAR Image Formation with Suppressing Multipath Ghosts," Radar, 2006. CIE '06. International Conference on, vol., no., pp.1-3, 16-19 Oct. 2006.

[15] Gesbert, D.; Shafi, M.; Da-shan Shiu; Smith, P.J.; Naguib, A.; , "From theory to practice: an overview of MIMO space-time coded wireless systems," *Selected Areas in Communications, IEEE Journal on* , vol.21, no.3, pp. 281- 302, Apr 2003

[16] Raleigh, G.G.; Cioffi, J.M.; , "Spatio-temporal coding for wireless communication," *Communications, IEEE Transactions on* , vol.46, no.3, pp.357-366, Mar 1998

[17] PAULRAJ, A.J.; GORE, D.A.; NABAR, R.U.; BOLCSKEI, H.; , "An overview of MIMO communications - a key to gigabit wireless," *Proceedings of the IEEE* , vol.92, no.2, pp. 198- 218, Feb 2004

[18] G. A. Gilmour. Synthetic aperture side-looking sonar system. Journal of the AcousticalSociety of America, 65(2):557, May 1978. Review of U.S. Patent 4,088,978.

[19] V. F. Mecca, D. Ramakrishnan, and J. L. Krolik, "MIMO radar space–time adaptive processing for multipath clutter mitigation," Proc. IEEE Workshop Sensor Array Multichannel Signal Processing, pp. 249–253, Jul. 2007

[20] Mecca, V.F.; Krolik, J.L.; Robey, F.C.; , "Beamspace slow-time MIMO radar for multipath clutter mitigation," *Acoustics, Speech and Signal Processing, 2008. ICASSP 2008. IEEE International Conference on* , vol., no., pp.2313-2316, March 31 2008-April 4 2008

[21] Mecca, V.F.; Krolik, J.L.; , "MIMO STAP clutter mitigation performance demonstration using acoustic Arrays," *Signals, Systems and Computers, 2008 42nd Asilomar Conference on* , vol., no., pp.634-638, 26-29 Oct. 2008

[22] M. Richards, Fundamentals of Radar Signal Processing, McGraw-Hill, 2005.

[23] M. Soumekh, Synthetic Aperture Radar Signal Processing with MATLAB Algorithms. New York: Wiley, 1999.

[24] Bamler, R.; , "A comparison of range-Doppler and wavenumber domain SAR focusing algorithms," *Geoscience and Remote Sensing, IEEE Transactions on* , vol.30, no.4, pp.706-713, Jul 1992

[25] Cumming, I.G.; Neo, Y.L.; Wong, F.H.; , "Interpretations of the omega-K algorithm and comparisons with other algorithms," *Geoscience and Remote Sensing Symposium, 2003. IGARSS '03. Proceedings. 2003 IEEE International* , vol.3, no., pp. 1455- 1458, 21-25 July 2003

[26] C. Cafforio, C. Prati, and F. Rocca, "SAR data focusing useing seismic migration techniques," IEEE Trans. Aerosp. Electron. Syst., vol. 27, pp. 199–207, Mar. 1991.

[27] Krieger, G.; Gebert, N.; Moreira, A.; , "Multidimensional Waveform Encoding: A New Digital Beamforming Technique for Synthetic Aperture Radar Remote

Sensing," *Geoscience and Remote Sensing, IEEE Transactions on* , vol.46, no.1, pp.31-46, Jan. 2008.

[28] Yu, J.; Krolik, J.; , "Quadrature slow-time MIMO radar with experimental results," *Signals, Systems and Computers (ASILOMAR), 2010 Conference Record of the Forty Fourth Asilomar Conference on* , vol., no., pp.2134-2137, 7-10 Nov. 2010.

[29] W. C. Chew. Waves and Fields in Inhomogeneous Media. IEEE Press, 1995.

[30] C. E. Cook and M. Bernfeld. Radar signals: an introduction to theory and application. Academic Press Inc., 1967.

[31] Bellettini, A.; Pinto, M.A.; , "Theoretical accuracy of synthetic aperture sonar micronavigation using a displaced phase-center antenna," *Oceanic Engineering, IEEE Journal of* , vol.27, no.4, pp. 780- 789, Oct 2002

[32] H. V. Trees, Optimum Array Processing. New York: Wiley, 2002.

[33] Yu, J.; Reynolds, M.; Krolik, J.; , "An indoor S-band radar receive array testbed," Radar Conference, 2010 IEEE , vol., no., pp.712-717, 10-14 May 2010.

[34] Li Li; Yu, J.; Krolik, J.; , "Software-defined calibration for FMCW phased-array radar," Radar Conference, 2010 IEEE , vol., no., pp.877-881, 10-14 May 2010.